

# Uniformly Spherical and Monodisperse Antimony- and Zinc-Doped Tin Oxide Nanoparticles for Optical and Electronic Applications

Riddhiman Medhi,<sup>†</sup> Chien-Hung Li,<sup>‡</sup> Sang Ho Lee,<sup>†</sup> Maria D. Marquez,<sup>†</sup> Allan J. Jacobson,<sup>†</sup> Tai-Chou Lee,<sup>§</sup> and T. Randall Lee<sup>\*,†</sup>

<sup>†</sup>Department of Chemistry and the Texas Center for Superconductivity, University of Houston, 4800 Calhoun Road, Houston, Texas 77204-5003, United States

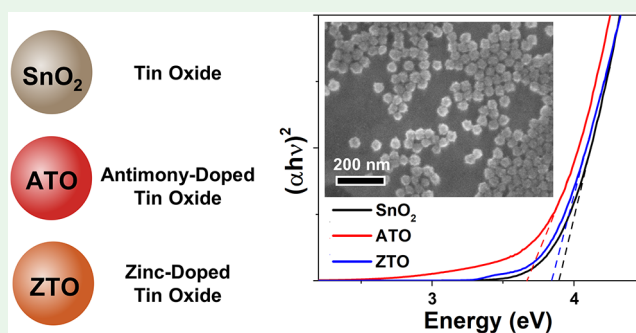
<sup>‡</sup>Department of Medicinal and Applied Chemistry, Kaohsiung Medical University, Kaohsiung 80708, Taiwan

<sup>§</sup>Department of Chemical and Materials Engineering, National Central University, 300 Jhongda Road, Jhongli City 32001, Taiwan

## S Supporting Information

**ABSTRACT:** Doping is an effective way to tune the band gap of metal oxide semiconductor materials. Doped tin oxide nanoparticles have proven to be effective materials for various electro-optical applications, particularly when deposited in thin-film architectures. However, doping in metal oxide nanoparticles generally leads to distorted shapes and a lack of uniformity, making the ready preparation of spherical, monodisperse doped tin oxide stand-alone nanoparticles an elusive task. This report describes a facile, solution-based method for the synthesis of stable, monodisperse antimony- and zinc-doped tin oxide nanoparticles, which opens the door to disperse these materials in a variety of media and expand their range of applications. The band gap of the tin oxide nanoparticles was successfully tuned upon doping with antimony and zinc. The tin-oxide-based nanomaterials were characterized using scanning electron microscopy (SEM), transmission electron microscopy (TEM), X-ray photoelectron spectroscopy (XPS), energy dispersive X-ray spectroscopy (EDX), and X-ray diffraction (XRD). Separately, the optical properties of the nanoparticles were evaluated by UV–vis diffuse reflectance spectroscopy (DRS) and photoluminescence spectroscopy (PL). These nanoparticles can be very effective in creating well-controlled systems for photocatalysis, solar cells, optoelectronics, multilayered devices, and for the treatment of air and water pollutants.

**KEYWORDS:** tin oxide, doped, antimony, zinc, SnO<sub>2</sub>, ATO, ZTO, semiconductor, photocatalyst



## INTRODUCTION

Heterogeneous metal oxide photocatalysts have been recognized as a valuable technology for numerous applications such as chemical synthesis, pollutant degradation in both air and water, antibacterial applications, UV filters, optoelectronics, and transparent self-cleaning coatings.<sup>1–5</sup> The photocatalytic activity of materials based on tin oxide (SnO<sub>2</sub>) has attracted particular attention because of their high mobility carrier properties, chemical stability across a wide range of pH values, and high photocatalytic activity.<sup>6</sup> In addition, tin oxide is unique in its dual ability for electrical conductivity and transparency, as demonstrated by its use in the fabrication of transparent conducting electrodes.<sup>7</sup> This unique combination of features has attracted considerable attention for various applications, such as gas sensors,<sup>8–11</sup> solar cells,<sup>12</sup> and transistors.<sup>13</sup> However, a major limitation regarding the use of bulk SnO<sub>2</sub>-based materials as photocatalysts is the confinement of their absorbance to only the UV region due to their large band gap. Bulk SnO<sub>2</sub> is an n-type semiconductor with a band gap,  $E_g$ , of 3.6 eV at 300 K, which corresponds to a

wavelength of 344 nm.<sup>14,15</sup> Thus, their optical activity is restricted to only 5% of the solar spectrum that reaches the surface of the earth. Notably for these materials, photocatalysis does not occur under daylight or conventional light sources, as UV wavelengths are not present, which restricts the practical uses of materials based on pure SnO<sub>2</sub> as photocatalysts.

Nonetheless, the band gap of tin oxide can be modified by introducing a wide range of dopants, which can lead to marked improvements in the chemical and physical properties of the materials. For example, literature reports demonstrate tuning of the band gap via the introduction of specific dopants to yield, for example, indium–tin oxide (ITO, 3.62–4.03 eV),<sup>16</sup> fluorine-doped tin oxide (FTO, 3.7–3.8 eV),<sup>17,18</sup> tungsten-doped tin oxide (WTO, 4.05–4.22 eV),<sup>19</sup> antimony-doped tin oxide (ATO 3.1–3.9 eV),<sup>20–23</sup> and zinc-doped tin oxide

**Received:** August 2, 2019

**Accepted:** September 25, 2019

**Published:** September 25, 2019

(ZTO, 3.58–3.97 eV).<sup>24,25</sup> The high cost associated with indium oxide, the most widely used doped tin oxide, has led to a demand for cost-effective replacements with similar or superior properties.

Two promising alternative candidates are tin oxides doped with antimony and zinc, which are thermally and chemically more stable than undoped SnO<sub>2</sub>.<sup>20,22,24–28</sup> For example, studies have shown that ATO films can exhibit high mobility, low resistivity (ranging from  $1.22 \times 10^{-3} \Omega \text{ cm}$  to  $5 \times 10^{-3} \Omega \text{ cm}$ ), and tunable band gaps (ranging from 3.9 to 3.1 eV) while maintaining transparency.<sup>20,21,23,27</sup> ATO thin films have also been shown to be promising sensors for NO<sub>x</sub> species.<sup>20</sup> Similarly, the band gap of ZTO films has also been tuned between 3.61 and 3.97 eV with some examples exhibiting low resistivity and high carrier mobilities of  $7.7 \text{ cm}^2/(\text{V s})$  in transistors.<sup>24–26,29</sup> Antimony and zinc, however, induce changes to the band structure of tin oxide by distinct mechanisms. The substitution of antimony atoms for tin atoms is analogous to tin doping in indium oxide to make indium tin oxide (ITO), which is widely used in flat-panel displays, touch screens, organic light-emitting diodes (OLEDs), and gas sensors.<sup>30–32</sup> Heavily doped antimony (>10%) tin oxide adds extra electrons to the system, which effectively shifts the Fermi level into the conduction band, significantly increasing the conductivity.<sup>33</sup> Antimony also adds donor levels below the original conduction band, which in turn leads to a reduction of the optical band gap.<sup>33</sup> The substitution of Sn<sup>4+</sup> ions with Zn<sup>2+</sup> ions, on the other hand, adds an acceptor energy level near the valence band, which leads to a reduced band gap in ZTO.<sup>29</sup> The enhancement in conductivity in ZTO is also mostly associated with a change in the highly conductive surface layer of SnO<sub>2</sub>, rather than a Fermi level shift in the entire material.<sup>29</sup> Thus, antimony and zinc both enhance the conductivity of tin oxide in different ways, while maintaining its transparency with a tunable optical band gap in the UV region.

Notably, ATO and ZTO have high carrier mobilities, good electrical conductivities, and excellent optical transmittance, making them two promising doped tin oxide materials to be studied on the nanoscale. Further tuning the band gap of SnO<sub>2</sub> materials has been achieved by utilizing various nanostructured materials, where changes in the band gap of nanoscale materials arises from quantum confinement; moving to nanoscale sizes also significantly increases the surface-to-volume ratio, a parameter beneficial for applications in catalysis and sensing.<sup>4,34</sup> Moreover, changes in the band structure of these materials on the nanoscale, through doping, allows for the tailoring of their properties to achieve specifically targeted applications.<sup>35</sup>

Another major drawback of traditional metal oxide photocatalysts is rapid electron–hole recombination,<sup>36,37</sup> where electrons excited into the conduction band radiatively recombine with holes, thus quenching the targeted reduction reaction.<sup>37</sup> Various methods have been employed to reduce the rate of electron–hole recombination in these traditional photocatalysts.<sup>38,39</sup> Doping was also seen to be an effective strategy to reduce the rate of electron–hole recombination in the case of nanosized TiO<sub>2</sub> photocatalysts.<sup>40,41</sup> Furthermore, cationic and anionic doping has been shown to reduce the rate of electron–hole recombination in some systems,<sup>40,42</sup> which can be attributed to the introduction of deep and shallow trap states induced by oxygen vacancies caused by doping.<sup>43</sup> In addition to enhancing the amount of accessible charge carriers,

the doping of metal oxide semiconductor nanostructures have also successfully improved hole-transfer kinetics for expedited photoactivity toward solar water splitting and organic degradation.<sup>44–46</sup> Thus, we envision that doping SnO<sub>2</sub> semiconductor nanoparticles with antimony and zinc will give rise to similar inhibition of electron–hole recombination and enhance their photochemical activity.

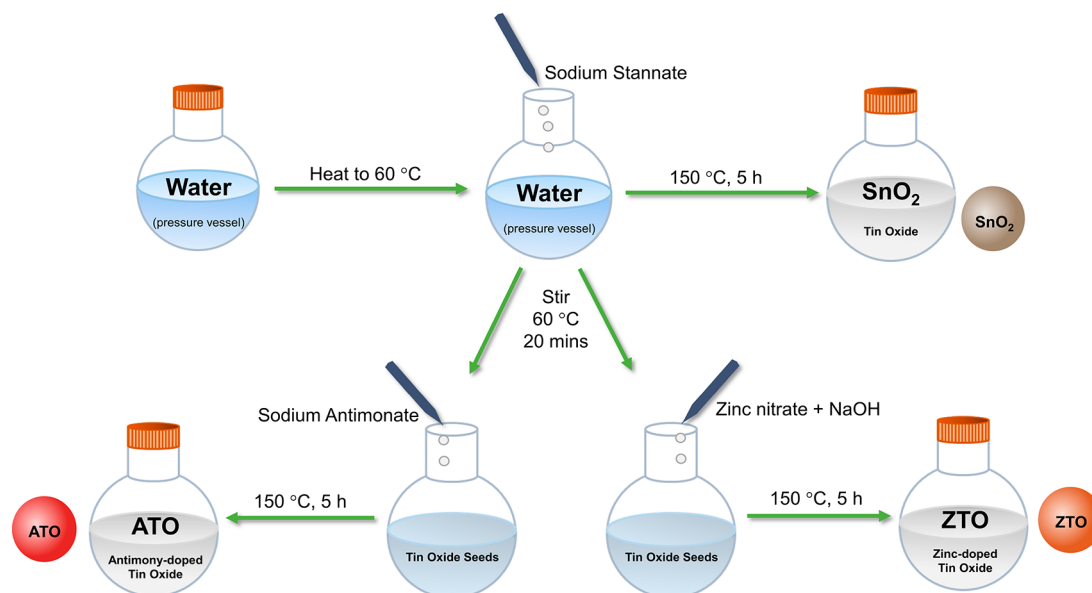
Simple and accessible synthetic methods are important not only for academic study but also for industrial use. Several methods have been used for the fabrication of SnO<sub>2</sub> nanoparticles, including precipitation,<sup>47,48</sup> thermal decomposition,<sup>49</sup> microwave-assisted,<sup>50</sup> and hydrothermal protocols.<sup>51–53</sup> However, the handful of reports that exist for SnO<sub>2</sub> nanoparticles are complicated and afford particles that are polydisperse with nonuniform morphologies.<sup>54–56</sup> Furthermore, the introduction of dopants into metal oxide nanoparticles remains a challenging task mainly due to the introduction of surface vacancies and defects, which renders the surface reactive and unstable to aggregation.<sup>57</sup> Although doped tin oxides have been shown to be effective materials as thin films, the ready preparation of spherical, monodisperse doped tin oxide stand-alone nanoparticles has eluded researchers because of the aforementioned reasons. Unlike thin films, stand-alone nanoparticles open the door to disperse these materials in a variety of media to expand their range of applications; for example, they can be deposited onto substrates to make sensors, solar cells, electrodes, smart windows, multilayered devices, and light-emitting diodes (LEDs). They can also be dissolved in solutions and gels for UV absorption filters, photocatalysis, antibacterial applications, as well as for treating contaminated air and water.

Therefore, in this study, we report a facile and effective one-step surfactant-free solution-based method for the synthesis of stand-alone, monodisperse, and uniformly spherical SnO<sub>2</sub>, antimony-doped, and zinc-doped SnO<sub>2</sub> (ATO and ZTO, respectively) nanoparticles. Furthermore, our method successfully demonstrates the ability to tune the band gap of the SnO<sub>2</sub> nanoparticles upon doping with zinc and antimony. All of the hybrid nanoparticles were characterized by scanning electron microscopy (SEM), transmission electron microscopy (TEM), dynamic light scattering (DLS), X-ray photoelectron spectroscopy (XPS), and X-ray diffraction (XRD). Separately, their optical properties were evaluated by diffuse reflectance UV–vis spectroscopy (DRS) and photoluminescence (PL) spectroscopy.

## ■ EXPERIMENTAL SECTION

**Materials.** Sodium stannate trihydrate and zinc nitrate were purchased from Sigma-Aldrich and used without further purification. Sodium antimonate trihydrate (Alfa Aesar) and sodium hydroxide (Flinn Scientific Inc.) were purchased from the indicated suppliers and used without modification. Water was purified to a resistance of 18 M $\Omega$ -cm (Academic Milli-Q Water System, Millipore Corporation). All glassware used during the experiments was cleaned in a base bath followed by piranha solution (3:1 H<sub>2</sub>SO<sub>4</sub>:H<sub>2</sub>O<sub>2</sub>) or aqua regia solution (3:1 HCl:HNO<sub>3</sub>) and then dried in the oven prior to use. *Caution: the latter reagents are dangerous and must be handled with care.*

**Characterization Methods.** The nanoparticles (NPs) were imaged using a scanning electron microscope (SEM, LEO-1525) operating at an accelerating voltage of 15 kV. All SEM samples were deposited on a silicon wafer washed with water and ethanol. For improved resolution, the NPs were also evaluated using a JEM-2000 FX transmission electron microscope (TEM) and JEOL JEM-2010

Scheme 1. Synthesis of SnO<sub>2</sub>, ATO, and ZTO NanoparticlesTable 1. Reaction Parameters used for the Synthesis of SnO<sub>2</sub>, ATO, and ZTO Nanoparticles

particle	water	40 mM Na <sub>2</sub> Sn <sub>2</sub> O <sub>3</sub>	final temperature	reaction time <sup>a</sup>	NaSbO <sub>3</sub> ·3H <sub>2</sub> O solution	zinc precursor	centrifuge (speed, time)
SnO <sub>2</sub>	20 mL	3 mL	150 °C	5 h	-	-	7000 rpm, 30 min
ATO	20 mL	3 mL	150 °C	5 h	10 mL <sup>b</sup>	-	7000 rpm, 30 min
ZTO	20 mL	3 mL	150 °C	5 h	-	0.4 mL	7000 rpm, 30 min

<sup>a</sup>Reaction time at final temperature. <sup>b</sup>0.0496 g of NaSbO<sub>3</sub>·3H<sub>2</sub>O was used to prepare the sodium antimonate solution for the ATO nanoparticles.

TEM, both operating at an accelerating voltage of 200 kV. All TEM samples were deposited on 300-mesh holey carbon-coated copper grids and dried overnight before analysis. Dynamic light scattering (DLS) measurements were conducted using a Malvern Zetasizer Nano ZS. X-ray diffraction (XRD) measurements were obtained using a X'PERT PRO PANalytical X-ray diffractometer using Cu K $\alpha$  radiation over the  $2\theta$  range of 20°–100°. A concentrated sample of the nanoparticles in water was deposited on a piranha-cleaned glass slide prior to XRD analysis. The collected XRD data were analyzed using the PANalytical HighScore Plus software. The background glass peak was subtracted, and the resulting patterns were analyzed for sample peaks. The exact peak positions and fwhm values used for crystallite size measurements were used as provided by the software. Crystallite size calculations were conducted using the Scherrer equation.<sup>16</sup> X-ray photoelectron spectroscopy (XPS) data were collected using a PHI 5700 X-ray photoelectron spectrometer equipped with a monochromatic Al K $\alpha$  source with 10 mA emission current and 15 kV emission bias. Concentrated samples of the nanoparticles in water were dropped on copper-tape-covered silicon wafers and dried overnight in a vacuum desiccator prior to analysis with XPS. Before sample preparation, the copper-tape-covered slides were washed with Milli-Q water followed by ethanol several times before being dried with nitrogen gas. A neutralizer was used during XPS measurement, and all spectra were standardized with respect to the Sn peak at 486 eV. Energy-dispersive X-ray spectroscopy (EDX) data were collected at 18 kV by an EDX attached to a Nova NanoSEM 230 microscope, providing the elemental composition of the particles. Diffuse reflectance spectra (DRS) were obtained in the powdered solid state using a Cary 5000 UV–vis NIR spectrometer from Agilent Technologies. Photoluminescence measurements were performed using a PerkinElmer LS55 fluorometer; an excitation wavelength of 315 nm and a cutoff filter at 390 nm were used to ensure complete excitation and minimize spectral noise.

**Synthesis of the Nanoparticles.** Scheme 1 illustrates the synthetic strategy taken to synthesize the tin oxide (SnO<sub>2</sub>),

antimony-doped tin oxide (ATO), and zinc-doped tin oxide (ZTO) nanoparticles.

**Synthesis of SnO<sub>2</sub> Nanoparticles.** The synthetic strategy shown in Scheme 1 for preparing the SnO<sub>2</sub> nanoparticles was adapted from methods reported previously.<sup>53,58,59</sup> Reagent amounts, reaction times, temperatures used, and centrifugation parameters are detailed in Table 1. In general, water was heated in a round-bottom flask to 60 °C and stirred vigorously, followed by the rapid addition of a 40 mM sodium stannate trihydrate solution. The mixture was heated to 150 °C for 5 h. The initially colorless solution turned white, indicating the formation of SnO<sub>2</sub> nanoparticles. All of the colloidal particles were collected by centrifugation and washed with deionized water to remove any unreacted species and impurities. This recipe was successfully scaled up 10-fold by using a 0.4 M rather than of 40 mM sodium stannate solution, while keeping all other parameters the same. This scaled-up recipe generated ~0.4 g of SnO<sub>2</sub> nanoparticles per batch.

**Synthesis of ATO Nanoparticles.** As detailed in Table 1, 20 mL of water was placed in a 75 mL glass pressure vessel and heated to 60 °C. Then, 40 mM Na<sub>2</sub>Sn<sub>2</sub>O<sub>3</sub> solution was added, and the contents were stirred for 20 min at 60 °C. Concurrently, NaSbO<sub>3</sub>·3H<sub>2</sub>O (0.0496 g, 0.201 mmol) was dissolved in 10 mL of water and heated to 90 °C to assist in dissolving the antimonate salt. The amount of NaSbO<sub>3</sub>·3H<sub>2</sub>O can be varied between 0.0124 and 0.0496 g to adjust the percentage of antimony doped within the tin oxide lattice. Specific amounts of the prepared NaSbO<sub>3</sub>·3H<sub>2</sub>O solution were mixed into the sodium stannate reaction mixture at 60 °C followed by sealing of the glass pressure vessel. Finally, the mixture was heated at 150 °C for an additional 5 h. The solution was then allowed to cool to room temperature followed by centrifugation. The supernatant was removed, and the residue was washed with water once and finally redispersed in Milli-Q water. This recipe was also successfully scaled up 5-fold using a 0.2 M sodium stannate solution and 0.0748 g of NaSbO<sub>3</sub>·3H<sub>2</sub>O precursor dissolved in 10 mL of water, while keeping all other parameters the same. This scaled-up recipe afforded ~0.2 g of ATO nanoparticles per batch.

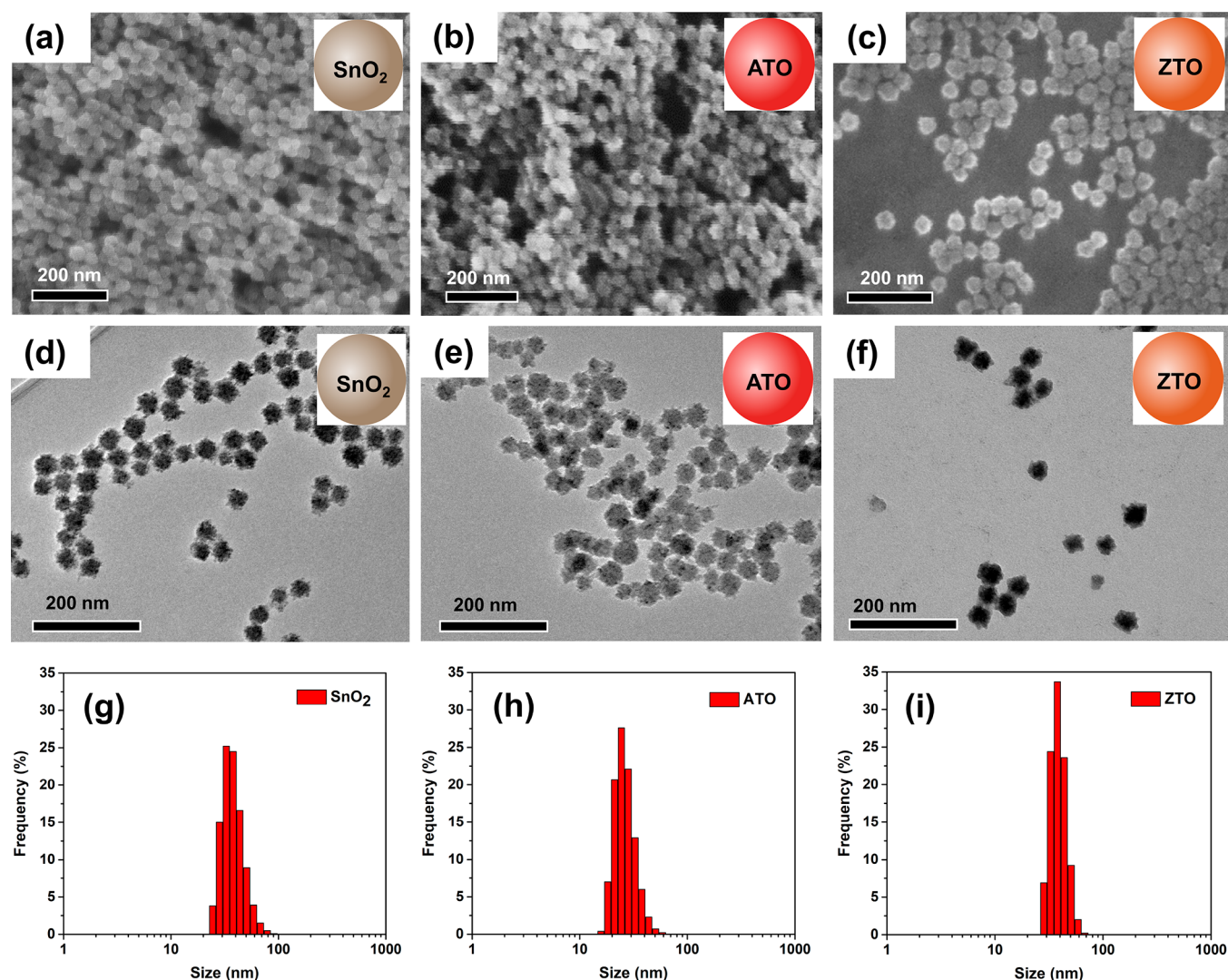


**Figure 1.** (a–c) SEM images and (d–f) TEM images of SnO<sub>2</sub>, ATO, and ZTO nanoparticles, respectively. (g–i) Size distribution of SnO<sub>2</sub>, ATO, and ZTO nanoparticles from DLS measurements.

**Synthesis of ZTO Nanoparticles.** As detailed in Table 1, 20 mL of water was placed in a 75 mL glass pressure vessel and heated to 60 °C. After the solution reached 60 °C, the specified amounts of 40 mM Na<sub>2</sub>SnO<sub>3</sub> solution were added, and the contents were stirred for 20 min. Concurrently, Zn(NO<sub>3</sub>)<sub>2</sub>·6H<sub>2</sub>O (0.095 g, 0.319 mmol) was dissolved in 5 mL of H<sub>2</sub>O. This solution was added to 0.5 mL of a 1 M NaOH solution to form a white zinc hydroxide, Zn(OH)<sub>2</sub>, precipitate. In a second step, an excess amount of base, in the form of 4.0 mL of a 1 M NaOH solution, was added to dissolve the Zn(OH)<sub>2</sub> precipitate to form a Na<sub>2</sub>ZnO<sub>2</sub> stock solution. The specified amount of this Na<sub>2</sub>ZnO<sub>2</sub> stock solution was then added to the sodium stannate reaction mixture at 60 °C, and the glass pressure vessel was resealed. Finally, the mixture was heated at 150 °C for an additional 5 h. The solution was then allowed to cool to room temperature followed by centrifugation. The supernatant was removed, and the residue was washed with water once and finally redispersed in Milli-Q water. This recipe was also successfully scaled up 5-fold using a 0.2 M sodium stannate solution and 2 mL of the prepared sodium zincate stock solution, while keeping all other parameters the same. This scaled-up recipe also afforded ~0.2 g of nanoparticles per batch.

## RESULTS AND DISCUSSION

### Synthesis and Morphology of the Nanoparticles.

Based on previous reports,<sup>53,58,59</sup> we designed a one-step

surfactant-free hydrothermal method to generate SnO<sub>2</sub> and doped SnO<sub>2</sub> nanoparticles (see Scheme 1). During the syntheses, we found that at temperatures above 57 °C, the colorless, transparent sodium stannate solution turned white, an indication of the formation of SnO<sub>2</sub> nanoparticles.<sup>60</sup> In aqueous solution, Na<sub>2</sub>SnO<sub>3</sub> readily dissociates to form Na<sup>+</sup> and Sn(OH)<sub>6</sub><sup>2-</sup> ions because of their high stability.<sup>60</sup> Previous studies have also shown that the pH of a sodium stannate solution typically decreases with an increase in temperature.<sup>60</sup> Since crystalline SnO<sub>2</sub> is the most stable phase at pH values lower than 11.7,<sup>60,61</sup> the formation of SnO<sub>2</sub> can be achieved from a sodium stannate solution at pH values <11. Utilizing this principle, we added 3 mL of an aqueous 0.04 M sodium stannate precursor solution (pH ~12) to 20 mL of water warmed at 60 °C, which led to a drop in pH from ~12 to ~10.5 and thus the formation of SnO<sub>2</sub> nanoparticles. We also found that the minimum temperature needed to obtain SnO<sub>2</sub> using our method is 60 °C, but the overall yield of particles was low at this temperature and reaction time. To increase the yield and crystallinity of the nanoparticles, we increased the temperature of the reaction to 150 °C and continued the reaction at this temperature for 5 h. The obtained undoped SnO<sub>2</sub> nanoparticles demonstrated a spherical morphology with

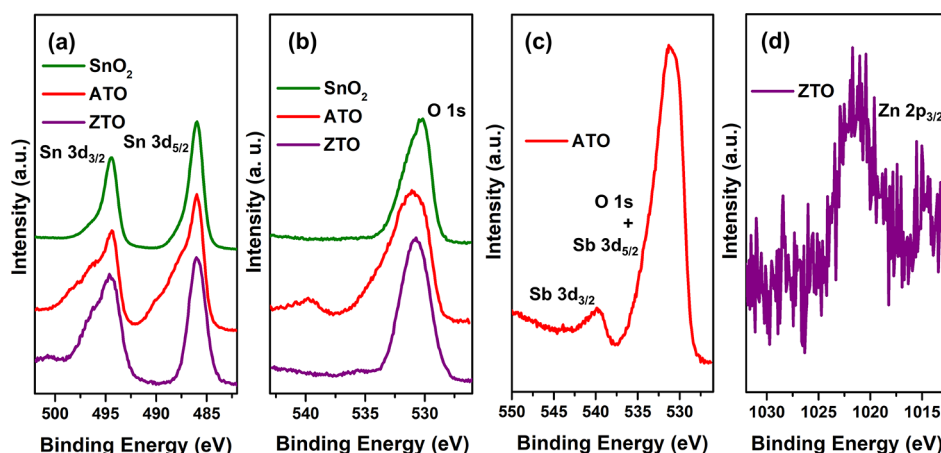


**Figure 2.** XPS spectra for (a) Sn 3d region for all nanoparticles, (b) O 1s region spectra for all nanoparticles, (c) Sb 3d region for the ATO nanoparticles, and (d) Zn 2p region for the ZTO nanoparticles.

**Table 2.** XPS-Derived Relative Atomic Concentration of Sn, Zn, and Sb in the Various Doped Tin Oxide Samples

sample	relative atomic concentration (%) <sup>a</sup>		
	Sn (3d <sub>5/2</sub> )	Zn (2p <sub>3/2</sub> )	Sb (3d <sub>5/2</sub> )
ATO	87 [area: 23558 counts]	---	13 [area: 3898 counts]
ZTO	91 [area: 22760 counts]	9 [area: 1270 counts]	---

<sup>a</sup>The XPS data are invariably dominated by oxygen, which has been removed from this table to offer a more meaningful representation of doping percentage. Measurements by XPS of our metal oxide nanoparticles typically show >80% oxygen.

good uniformity in shape and size (see SEM and TEM images in Figure 1; high-resolution TEM (HRTEM) images are provided in Figure S1). Our synthesis of SnO<sub>2</sub> nanoparticles is scalable up to 10-fold (using a 0.4 M solution of Na<sub>2</sub>SnO<sub>3</sub> rather than a 0.04 M solution) with little or no impact on homogeneity and shape; the only difference was a slight increase in the average size of the particles, from ~32 nm to ~40 nm (see also Figure S2a).

Doping with antimony and zinc was achieved using solutions of sodium antimonate and sodium zincate, respectively, together with the sodium stannate solution in a pressure vessel at 150 °C for 5 h. We observed during the course of our studies that the use of sealed vessels at 150 °C reaction temperatures led to improved crystallinity for all the tin oxide materials. Since sodium antimonate is sparingly soluble in water, a higher initial temperature of ~90 °C was required to prepare its aqueous solution prior to addition into the sodium stannate reaction mixture. The final temperature of 150 °C in the pressure vessel ensures further dissolution of the sodium antimonate and subsequent introduction of antimony into the tin oxide lattice. Separately, the aqueous sodium zincate precursor solution was prepared from a mixture of zinc nitrate and sodium hydroxide. Doping was confirmed using XPS, EDX, and XRD and are discussed in detail in later sections. Similar to the synthesis of the undoped SnO<sub>2</sub> nanoparticles, the syntheses of ATO and ZTO nanoparticles are scalable up to 5-fold as described in the Experimental Section, with little or no effect on homogeneity and shape; the only notable difference in the two methods was an increase in the average size from ~35 nm to ~40 nm upon scaleup (see also Figure S2b,c).

Overall, this method proved to be reliable for the large-scale synthesis of homogeneous spherical SnO<sub>2</sub> nanoparticles in the size range of 30–35 nm with a slight increase to ~40 nm in the upscaled procedure. Analysis by SEM and TEM images

showed that even in the absence of surfactant, the SnO<sub>2</sub> nanoparticles were spherical and colloidal dispersed, with uniform sizes (see Figures 1, S1 and S2). The average diameter of the SnO<sub>2</sub>, ATO, and ZTO nanoparticles was 32 ± 3, 31 ± 4, and 39 ± 3 nm, respectively, as determined by SEM and TEM image analysis. The small standard deviations (≤4 nm) confirm the monodisperse nature of the synthesized nanoparticles. Size distribution histograms obtained from dynamic light scattering (DLS) measurements, as shown in Figure 1g–i, also demonstrate similar dimensions for the nanoparticles. The ATO nanoparticles were the smallest, while the ZTO nanoparticles showed the narrowest size distribution among the three. These DLS results correspond well with the trends observed in the SEM and TEM imaging.

**Composition and Structural Analysis.** Analysis by XPS was performed to determine the atomic composition at or near the surface of the particles (see Figure 2 and Table 2). The oxygen peaks at ~530.0 eV are consistent with the presence of tin oxide; moreover, strong Sn 3d<sub>5/2</sub> and Sn 3d<sub>3/2</sub> peaks at 486.0 and 494.5 eV, respectively, are consistent with the presence of tin (see Figure 2a,b). For the doped nanoparticles, the Sn 3d<sub>5/2</sub> and Sn 3d<sub>3/2</sub> peaks are broader, likely due to oxygen vacancies. For the ATO nanoparticles, the Sb 3d<sub>5/2</sub> peak overlaps with the oxygen 1s peak. However, the observation of a significant Sb 3d<sub>3/2</sub> peak conclusively demonstrated the presence of antimony (Figure 2c). Quantitative analysis for antimony was complicated by the presence of the O 1s peak. Calculation of antimony intensity in the presence of oxygen has been described in detail in the work by Garbasi.<sup>62</sup> We adopted this approach to calculate the amount of antimony in our samples. Because of spin orbit coupling, the antimony Sb 3d peak splits into a doublet composed of 3d<sub>5/2</sub> and 3d<sub>3/2</sub> in the ratio 3:2 or ~1.5 with respect to intensity (area). The Sb 3d<sub>5/2</sub> peak overlaps with the oxygen 1s peak, but the Sb 3d<sub>3/2</sub> peak can be clearly observed.

Consequently, we used the Sb  $3d_{3/2}$  peak intensity multiplied by 1.5 to obtain the area under the Sb  $3d_{5/2}$  peak, which was then used to calculate the Sb composition. The quantitative analysis revealed that the Sb doping with respect to Sn in the tin oxide lattice was 13% (Table 2), which is a doping ratio similar to commercially available ATO nanomaterials.<sup>54</sup> Theoretical studies conducted by Lu et al. have shown that doping of  $\sim 13\%$  antimony in tin oxide shifts the Fermi level into the conduction band contributed by the s and p orbitals of Sn and Sb atoms.<sup>33</sup> Typically, this doping percentage is within the range required for triggering good conductivity while retaining optical transparency in heavily doped wide band gap semiconductors such as ITO and ATO.<sup>31,33,54</sup>

The ZTO nanoparticles exhibited a Zn  $2p_{3/2}$  peak at 1021.0 eV, indicating the presence of  $Zn^{2+}$  in the structure (Figure 2d). According to studies conducted by Jiang et al., ZTO structures with  $\sim 10\%$  zinc doping exhibited the lowest resistivity and highest carrier concentration out of the several doping amounts studied;<sup>29</sup> consequently, our goal was to obtain ZTO particles with  $\sim 10\%$  zinc doping. Quantitative analysis of the Sn  $3d_{5/2}$  and Zn  $2p_{3/2}$  peaks revealed that the Zn doping in the measured samples with respect to Sn in the tin oxide lattice was 9% (Table 2). Jiang et al. also pointed out that the increase in conductivity of ZTO arises from the surface conduction of tin oxide.<sup>29</sup> As such, because of a greater surface-to-bulk ratio, the conductivity of ZTO films increase as the films become thinner.<sup>29</sup> The synthesis of  $\sim 40$  nm ZTO nanoparticles with 9% doping as described herein opens the door to the fabrication of ultrathin ZTO films with high conductivity for use in gas-sensing applications.

Importantly, our synthesis procedure allows us to control the percentage of Zn and Sb by varying the amount of sodium zincate and sodium antimonate added during the synthesis. The dopant concentration was readily controllable in the case of the ATO NPs:  $\sim 3\%$ ,  $\sim 6\%$ ,  $\sim 8\%$ , and  $\sim 13\%$  Sb doping in the ATO NPs was obtained by varying the amount of sodium antimonate salt (0.0124, 0.00248, 0.0372, and 0.0496 g, respectively). Similarly, we achieved doping percentages of  $\sim 4\%$  and  $\sim 9\%$  zinc by using 0.2 and 0.4 mL of the zinc precursor solution, respectively. Subsequent discussions focus predominantly on the 13% doped ATO and 9% doped ZTO nanoparticles as these particles offer the most promising applications according to previous reports.<sup>29,33,54</sup>

In a complementary effort to evaluate the degree of doping, we employed SEM-EDX to determine the elements present in the various  $SnO_2$ , ATO, and ZTO nanoparticles. The SEM-EDX spectra of the nanoparticles are shown in Figure 3a–c. All of the samples were deposited onto silicon wafers coated with copper tape. The SEM-EDX spectra show that all of the nanoparticles contained peaks characteristic for Sn  $L\alpha$  and M at 3.44 and 0.69 eV, respectively. In addition, oxygen  $K\alpha$  peaks at 0.525 eV were observed for all of the nanoparticles. Notably, Sb has peaks that overlap with those of Sn due to their close proximity in the periodic table. Nevertheless, in the spectrum of the ATO nanoparticles (Figure 3b), the characteristic peaks for Sb  $L\alpha$  and M can be observed at 3.60 and 0.73 eV, respectively. Furthermore, the peaks attributable to Sb in the ATO nanoparticles become evident upon comparison with the spectrum of the undoped  $SnO_2$  nanoparticles (Figure 3a). Similarly, the SEM-EDX spectrum of the ZTO nanoparticles in Figure 3c reveal peaks for zinc  $K\alpha$  and  $L\alpha$  at 8.63 and 1.01 eV, respectively. On the whole, the SEM EDX data indicate doping percentages of 14% Sb in the ATO nanoparticles and 6% Zn in

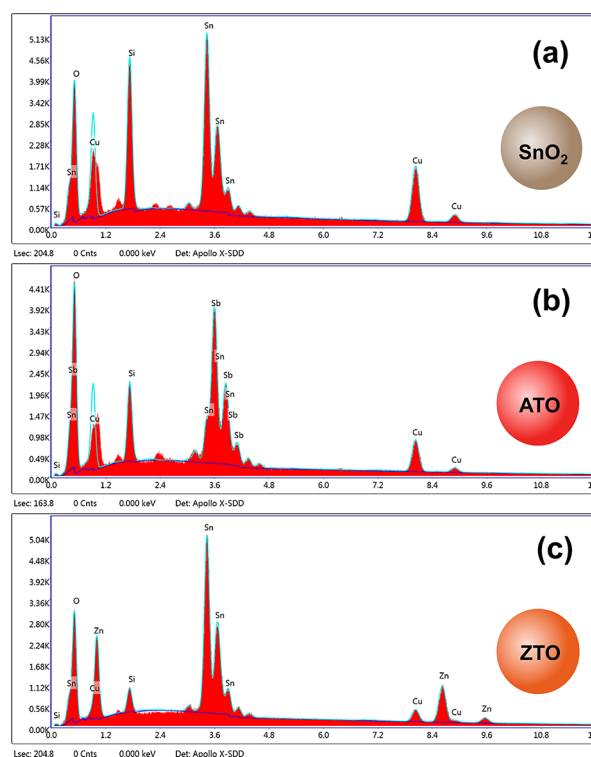


**Figure 3.** SEM-EDX spectra of the (a)  $SnO_2$ , (b) ATO, and (c) ZTO nanoparticles.

the ZTO nanoparticles, which are consistent with the XPS data and confirm the composition throughout the nanoparticles rather than only on their surface.

The EDX-mapping images are presented in the Supporting Information (Figure S3) and show Sn and O signals from areas on the wafer where there is an abundant deposition of the  $SnO_2$  nanoparticles. For the ATO and ZTO nanoparticles (Figures S4 and S5), the Sb and Zn signal intensities, respectively, mirror those of Sn. As such, the EDX studies as a whole confirm the successful distribution of the dopant metals in the  $SnO_2$  nanoparticles. Important to note are the Cu  $K\alpha$  and  $L\alpha$  peaks at 8.04 and 0.93 eV, respectively, from the sample slides. The EDX-mapping reveals that the Cu is mostly detected from the areas on the wafer with sparse distribution of the nanoparticles, consistent with these peaks arising from the Cu-covered Si wafer. The Si peaks in the spectra probably arise from wafer particulates or the tweezers used to handle the samples.

Powder XRD patterns were collected to determine the phases present in the nanoparticles (see Figure 4). The XRD pattern for the  $SnO_2$  nanoparticles shows peaks at Bragg angles  $2\theta = 26.25^\circ$ ,  $34.19^\circ$  and  $51.51^\circ$ , which can be attributed to (110), (101), and (211) crystalline planes, respectively, indicating the presence of a tin oxide rutile phase (JCPDS 77–0451) with lattice constants  $a = b = 0.4794$  nm and  $c = 0.3128$  nm.<sup>47,49,52,63–67</sup> The high-resolution transmission electron microscopy (HRTEM) images of  $SnO_2$  (Figure S1) nanoparticles demonstrate their polycrystalline nature. The (110), (101), and (211) crystalline planes with  $d$ -spacing of 0.33, 0.26, and 0.18 nm, respectively, are apparent in the HRTEM image (Figure S1g), which further confirms the presence of rutile  $SnO_2$  phase. The ATO nanoparticles exhibited an XRD peak pattern similar to that of the undoped  $SnO_2$  nanoparticles, which is reasonable given that the sample

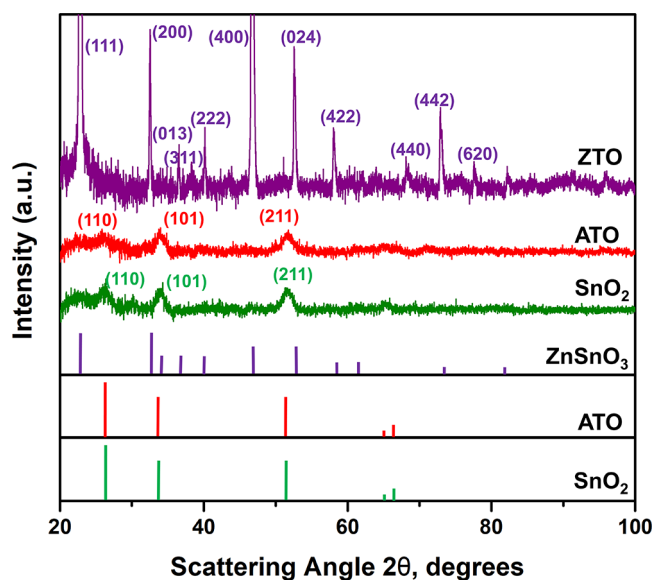


**Figure 4.** Powder XRD patterns for SnO<sub>2</sub>, ATO, and ZTO nanoparticles with their respective reference line patterns.

is composed of SnO<sub>2</sub> with Sb doped onto it. The similar peak pattern for the ATO nanoparticles is consistent with the literature for an ATO phase (JCPDS 21-1251).<sup>23,27,68,69</sup> The ATO nanoparticles exhibited XRD peaks at Bragg angles  $2\theta = 26.04^\circ$ ,  $33.95^\circ$ , and  $51.64^\circ$  which can be attributed to the (110), (101), and (211) crystalline planes, respectively. Importantly, the XRD data indicate that the SnO<sub>2</sub> rutile structure was maintained even after substitution of Sn<sup>4+</sup> ions with Sb<sup>5+</sup> ions in the lattice, although the lattice constants of the ATO nanoparticles differed slightly from those of the SnO<sub>2</sub> nanoparticles ( $a = b = 0.4839$  nm and  $c = 0.3150$  nm). Considering, however, the broadness of the peaks, this difference is arguably within the scope of experimental error. Imaging by HRTEM also confirms the similarity in the lattices (see Figure S1); the (110), (101), and (211) crystalline planes with  $d$ -spacing of 0.33, 0.26, and 0.18 nm, respectively, closely match those observed for SnO<sub>2</sub> nanoparticles. The XRD patterns, when coupled with the SEM-EDX mapping above, allows us to conclude that the antimony is doped into the tin oxide lattice with only antimony-doped tin oxide present and no other possible antimony species (e.g., the precursor sodium antimonate).

In contrast to doping with antimony, the XRD pattern of the ZTO nanoparticles showed the presence of a ZnSnO<sub>3</sub> phase<sup>70,71</sup> (JCPDS 11-0274), which indicates a change in the crystal structure of the tin oxide phase upon doping with zinc, also in accordance with previous literature.<sup>70</sup> Bragg angle peaks at  $2\theta = 22.78^\circ$ ,  $32.51^\circ$ ,  $36.57^\circ$ ,  $38.32^\circ$ ,  $40.15^\circ$ ,  $46.60^\circ$ ,  $52.54^\circ$ ,  $58.07^\circ$ ,  $68.29^\circ$ ,  $72.91^\circ$ , and  $77.66^\circ$  can be attributed to (111), (200), (013), (311), (222), (400), (024), (422), (440), (442), and (620) crystalline planes, respectively, which is consistent with a ZnSnO<sub>3</sub> phase.<sup>71</sup> The change in crystal structure of the SnO<sub>2</sub> upon doping with zinc can be attributed to the larger size of the Zn<sup>2+</sup> ions (74 pm) compared with Sn<sup>4+</sup> (69 pm) and Sb<sup>5+</sup> (60 pm).<sup>72</sup> Additionally, the sharp peaks observed in the XRD patterns of the ZTO particles is consistent with enhanced crystallinity for the ZTO nanoparticles when compared with the SnO<sub>2</sub> and ATO nanoparticles.

To confirm this conclusion, we performed crystallite size calculations using the Scherrer equation based on the XRD

data (see Table S1). The crystallite size for the ZTO nanoparticles was calculated to be 36 nm, while the crystallite sizes for the SnO<sub>2</sub> and ATO nanoparticles were calculated to be 7 and 6 nm, respectively. These calculations indicate that the SnO<sub>2</sub> and ATO nanoparticles are comprised of multiple smaller crystallites, which is consistent with the HRTEM imaging (Figure S1d–f), where the rough morphology is consistent with the small crystallite composition. In contrast, the largely monocrystalline ZTO nanoparticles exhibit a more homogeneous morphology, as observed in the SEM and TEM images (Figure 1). In addition, the crystallographic planes (111), (200), (400), and (024), corresponding to a ZnSnO<sub>3</sub> phase can be readily observed in the HRTEM images of the ZTO nanoparticles, further confirming their high degree of crystallinity.

**Optical Properties.** The optical band gaps of the tin oxide materials were determined using diffuse reflectance spectroscopy (Figure 5) and the Tauc equation (eq 1).

$$\alpha h\nu = A(h\nu - E_g)^r \quad (1)$$

To collect the diffuse reflectance spectra in the solid state, the nanoparticle solutions were centrifuged and then dried. Figure

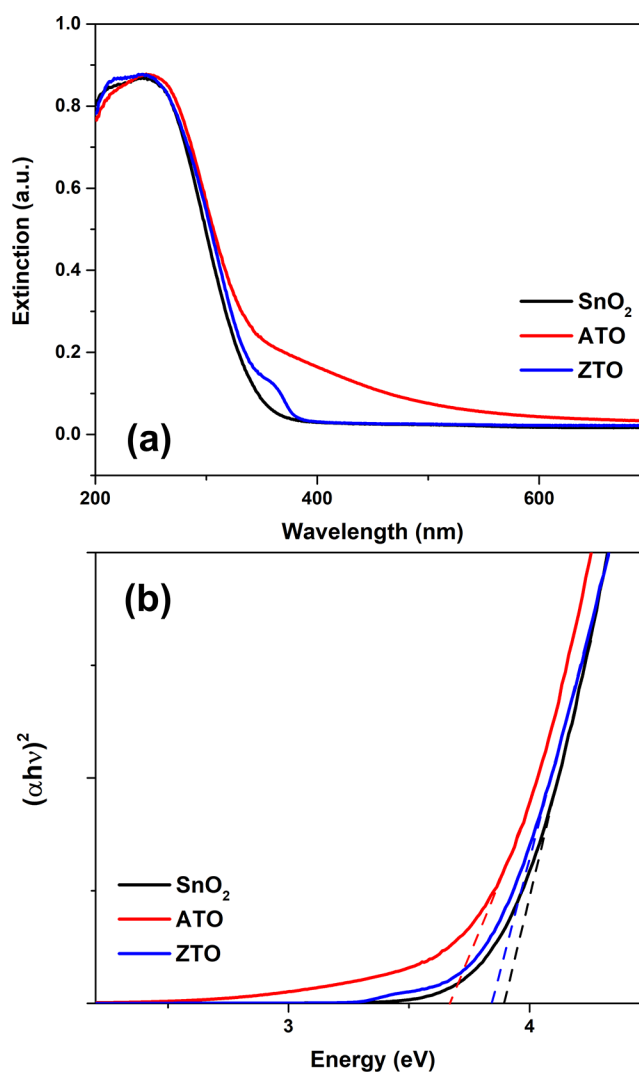


**Figure 5.** (a) Solid-state diffuse reflectance spectra and (b) Tauc plot for the SnO<sub>2</sub>, ATO, and ZTO nanoparticles.

Sa shows that the spectrum of the SnO<sub>2</sub> nanoparticles is characteristic of a wide band gap semiconductor, which is consistent with previous literature.<sup>73</sup> The relation between the absorption coefficients ( $\alpha$ ) and the incident photon energy ( $h\nu$ ) was used to calculate the optical band gap ( $E_g$ ) using eq 1.<sup>74</sup> The plots of  $(\alpha h\nu)^{1/r}$  (where  $r = 1/2$  for a direct band gap semiconductor)<sup>52</sup> versus photon energy ( $h\nu$ ) are shown in Figure 5b. The optical band gap of the SnO<sub>2</sub> nanoparticles was found to be 3.89 eV, which is slightly larger than the band gap of bulk SnO<sub>2</sub>, an expected result due to quantum confinement.<sup>75</sup>

Doping a metal oxide generally reduces the band gap due to the introduction of either donor or acceptor levels into the original band gap.<sup>76</sup> Accordingly, we observed a significant narrowing of the band gap and an enhancement in the visible absorption upon doping with antimony. In Figure 5, the diffuse reflectance spectrum and Tauc plot of the ATO nanoparticles suggest band bending upon doping, decreasing the band gap to 3.66 eV. The band edge shifted to a slightly higher wavelength, and in addition, there is a broad absorption tail extending up to 700 nm. Important to note is the slightly pale-yellow color of the ATO nanoparticles compared with the white-colored SnO<sub>2</sub> and ZTO nanoparticles; the color serves as another indication of greater visible light absorption by the ATO nanoparticles. Upon doping the SnO<sub>2</sub> nanoparticles with zinc, we observed a slight shift in the band edge to a higher wavelength region as the band gap decreased to 3.85 eV.

The origin of the small shoulder at 370 nm in the ZTO spectra is not known with certainty, but this peak has been observed in optical spectra for ZnO nanoparticles.<sup>77</sup> As such, this shoulder might plausibly arise from the presence of trace amounts of ZnO phases in the samples. We note, however, that the XRD results show no peaks for ZnO, which suggests that the amount of ZnO impurity phase, if any, is negligible compared to the primary ZTO phase. The band gap shift in ZTO is smaller than that observed upon doping with antimony, perhaps because of the restructuring of the crystal lattice triggered by doping with zinc (vide supra). However, it must be noted that the restructuring of the crystal lattice affords highly crystalline ZTO phases with long-range order, which should enhance other properties, such as electrical conductivity.<sup>78</sup>

Using an excitation wavelength of 315 nm, we collected photoluminescence (PL) spectra to examine the effect of doping on the rate of electron–hole recombination in tin oxide-based materials (see Figure 6). To provide meaningful comparisons, photoluminescence intensities were normalized with respect to particle concentration (Figure 6a) and volume percent of tin oxide material per particle (Figure 6b). The SnO<sub>2</sub> nanoparticles show a broad peak at 420–440 nm, with an apparently twinned peak at 422 and 437 nm; additionally, there are small shoulders at 454 and 496 nm. The spectra of the ZTO and ATO nanoparticles have similar characteristics as the spectrum of the SnO<sub>2</sub> nanoparticles. However, the exact peak positions of the ZTO nanoparticles match most closely to those of the SnO<sub>2</sub> nanoparticles. The spectrum of the ATO nanoparticles exhibited a slight red shift, with the twinned peaks appearing at 426 and 444 nm, and the shoulders appearing at 461 and 509 nm. The observed red shift might be attributed to the drastic shift in the band edge of the ATO nanoparticles compared with SnO<sub>2</sub> and ZTO nanoparticles.

Photoluminescence in semiconductor materials arises from the energy emitted during the electron–hole recombination

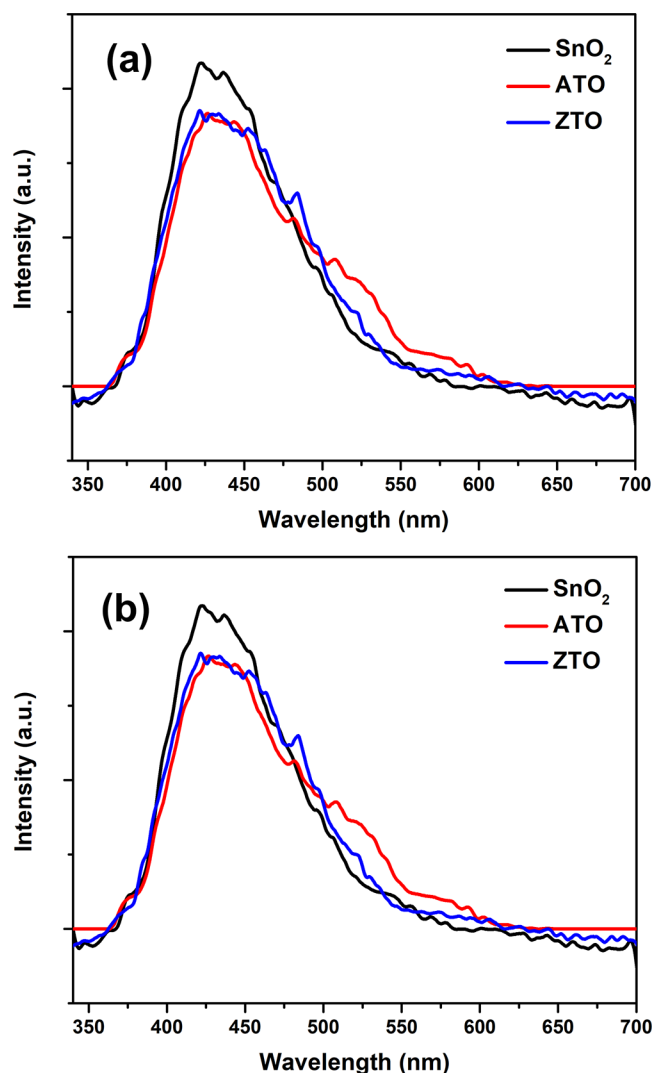


**Figure 6.** Photoluminescence spectra of SnO<sub>2</sub>, ATO, and ZTO nanoparticles normalized with respect to (a) particle concentration and (b) particle concentration and volume percentage of tin oxide material.

process. Consequently, a decrease in photoluminescence intensity is an indicator of inhibited electron–hole recombination.<sup>73</sup> In general for metal oxides, such a decrease in PL intensity is attributed to a decrease in oxygen vacancies or defects upon doping with a different metal.<sup>79</sup> In our nanoparticle samples, there is a decrease in the PL intensity upon doping with antimony and zinc compared with the undoped SnO<sub>2</sub> nanoparticles (i.e., there is an inhibition of electron–hole recombination upon doping with antimony and zinc). Along with the ability to tune the band gap, a decrease in the rate of electron–hole recombination makes Sb- and Zn-doped tin oxide nanoparticles attractive materials for diverse use in photocatalytic and photoelectronic applications. Specifically, the ATO nanoparticles, with enhanced visible light absorption, are good candidates for photocatalytic and photovoltaic use, while the ZTO nanoparticles, with their surface conductivity, will be useful materials for gas sensors.<sup>29,80</sup> Importantly, we demonstrate the ability to tailor the properties of tin oxide nanoparticles in multiple ways, thus expanding their scope of utilization.

## CONCLUSIONS

We demonstrated reliable surfactant-free hydrothermal-based routes to the synthesis of semiconductor nanoparticles comprised of tin oxide, antimony-doped tin oxide, and zinc-doped tin oxide, where the band gaps were tunable as a function of the dopant type and concentration. The protocols were scalable up to 0.2–0.4 g of nanoparticles per batch with a small increase in particle size and no effect on uniformity or monodispersity. Antimony doping of 13% was achieved in the ATO nanoparticles, while zinc doping was achieved at 9% in the ZTO nanoparticles. The band gap of the tin oxide nanoparticles (3.89 eV) was successfully tuned upon doping with antimony (e.g., 3.66 eV) and zinc (e.g., 3.85 eV). Photoluminescence measurements indicated a decrease in the rate of electron–hole recombination upon doping. The ability to easily synthesize stable, monodispersed SnO<sub>2</sub> particles, doped and undoped, with controllable uniformity of shape and size is important for various industrial and academic applications. On the whole, the doped nanoparticles, with tunable band gaps, offer advances in applications that include photocatalysis (e.g., water splitting), optoelectronic devices, gas sensors, and tunable electrodes for photoelectrochemical cells.

## ASSOCIATED CONTENT

### Supporting Information

The Supporting Information is available free of charge on the ACS Publications website at DOI: 10.1021/acsanm.9b01474.

Additional TEM and HRTEM imaging (Figure S1), SEM imaging (Figure S2), and SEM-EDX Mapping (Figures S3–S5) (PDF)

## AUTHOR INFORMATION

### Corresponding Author

\*E-mail: trlee@uh.edu (T.R.L.).

### ORCID

Riddhiman Medhi: 0000-0002-2368-2468

Allan J. Jacobson: 0000-0002-6540-8846

Tai-Chou Lee: 0000-0002-1695-1201

T. Randall Lee: 0000-0001-9584-8861

### Notes

A provisional patent application has been filed (U.S. Patent Application No. 62/799,432).

The authors declare no competing financial interest.

## ACKNOWLEDGMENTS

We thank the Air Force Office of Scientific Research (AFOSR FA9550-18-1-0094), the Robert A. Welch Foundation (Grant Nos. E-1320 and E-0024), and the Texas Center for Superconductivity for generously supporting this research. The authors would also like to thank Zhenglin Zhang and Weiguo Zhang for aiding with the PL and DRS measurements, respectively.

## REFERENCES

- (1) Yu, X.; Marks, T. J.; Facchetti, A. Metal Oxides for Optoelectronic Applications. *Nat. Mater.* **2016**, *15*, 383–396.
- (2) Raghunath, A.; Perumal, E. Metal Oxide Nanoparticles as Antimicrobial Agents: A Promise for the Future. *Int. J. Antimicrob. Agents* **2017**, *49*, 137–152.

- (3) Faustini, M.; Nicole, L.; Boissière, C.; Innocenzi, P.; Sanchez, C.; Grosso, D. Hydrophobic, Antireflective, Self-Cleaning, and Antifogging Sol–Gel Coatings: An Example of Multifunctional Nanostructured Materials for Photovoltaic Cells. *Chem. Mater.* **2010**, *22*, 4406–4413.

- (4) Ray, C.; Pal, T. Recent Advances of Metal–Metal Oxide Nanocomposites and their Tailored Nanostructures in Numerous Catalytic Applications. *J. Mater. Chem. A* **2017**, *5*, 9465–9487.

- (5) Lu, P. J.; Fang, S. W.; Cheng, W. L.; Huang, S. C.; Huang, M. C.; Cheng, H. F. Characterization of Titanium Dioxide and Zinc Oxide Nanoparticles in Sunscreen Powder by Comparing Different Measurement Methods. *J. Food Drug Anal.* **2018**, *26*, 1192–1200.

- (6) Lee, S. H.; Rusakova, I.; Hoffman, D. M.; Jacobson, A. J.; Lee, T. R. Monodisperse SnO<sub>2</sub>-Coated Gold Nanoparticles Are Markedly More Stable than Analogous SiO<sub>2</sub>-Coated Gold Nanoparticles. *ACS Appl. Mater. Interfaces* **2013**, *5*, 2479–2484.

- (7) Yu, S.; Li, L.; Xu, D.; Dong, H.; Jin, Y. Characterization of SnO<sub>2</sub>/Cu/SnO<sub>2</sub> Multilayers for High Performance Transparent Conducting Electrodes. *Thin Solid Films* **2014**, *562*, 501–505.

- (8) Harrison, P. G.; Willett, M. J. The Mechanism of Operation of Tin(IV) Oxide Carbon Monoxide Sensors. *Nature* **1988**, *332*, 337–339.

- (9) Shaalan, N. M.; Yamazaki, T.; Kikuta, T. NO<sub>2</sub> Response Enhancement and Anomalous Behavior of n-type SnO<sub>2</sub> Nanowires Functionalized by Pd Nanodots. *Sens. Actuators, B* **2012**, *166–167*, 671–677.

- (10) Shaalan, N. M.; Yamazaki, T.; Kikuta, T. Effect of Micro-Electrode Geometry on NO<sub>2</sub> Gas-Sensing Characteristics of One-Dimensional Tin Dioxide Nanostructure Microsensors. *Sens. Actuators, B* **2011**, *156*, 784–790.

- (11) Shaalan, N. M.; Yamazaki, T.; Kikuta, T. Influence of Morphology and Structure Geometry on NO<sub>2</sub> Gas-Sensing Characteristics of SnO<sub>2</sub> Nanostructures Synthesized via a Thermal Evaporation Method. *Sens. Actuators, B* **2011**, *153*, 11–16.

- (12) Tennakone, K.; Bandara, J.; Bandaranayake, P. K. M.; Kumara, G. R. A.; Konno, A. Enhanced Efficiency of a Dye-Sensitized Solar Cell Made from MgO-Coated Nanocrystalline SnO<sub>2</sub>. *Jpn. J. Appl. Phys.* **2001**, *40*, L732–L734.

- (13) Arnold, M. S.; Avouris, P.; Pan, Z. W.; Wang, Z. L. Field-Effect Transistors Based on Single Semiconducting Oxide Nanobelts. *J. Phys. Chem. B* **2003**, *107*, 659–663.

- (14) Mi, Y.; Odaka, H.; Iwata, S. Electronic Structures and Optical Properties of ZnO, SnO<sub>2</sub> and In<sub>2</sub>O<sub>3</sub>. *Jpn. J. Appl. Phys.* **1999**, *38*, 3453–3458.

- (15) Boulainine, D.; Kabir, A.; Bouanane, I.; Boudjema, B.; Schmerber, G. Oxidation Temperature Dependence of the Structural, Optical and Electrical Properties of SnO<sub>2</sub> Thin Films. *J. Electron. Mater.* **2016**, *45*, 4357–4363.

- (16) Senthilkumar, V.; Senthil, K.; Vickraman, P. Microstructural, Electrical and Optical Properties of Indium Tin Oxide (ITO) Nanoparticles Synthesized by Co-Precipitation Method. *Mater. Res. Bull.* **2012**, *47*, 1051–1056.

- (17) Banyamin, Y. Z.; Kelly, J. P.; West, G.; Boardman, J. Electrical and Optical Properties of Fluorine Doped Tin Oxide Thin Films Prepared by Magnetron Sputtering. *Coatings* **2014**, *4*, 732–746.

- (18) Obaida, M.; Moussa, I.; Boshra, M. Low Sheet Resistance F-Doped SnO<sub>2</sub> Thin Films Deposited by Novel Spray Pyrolysis Technique. *Int. J. ChemTech Res.* **2015**, *8*, 239–247.

- (19) Huang, Y.; Li, G.; Feng, J.; Zhang, Q. Investigation on Structural, Electrical and Optical Properties of Tungsten-Doped tin Oxide Thin Films. *Thin Solid Films* **2010**, *518*, 1892–1896.

- (20) Giralidi, T. R.; Escote, M. T.; Maciel, A. P.; Longo, E.; Leite, E. R.; Varela, J. A. Transport and Sensors Properties of Nanostructured Antimony-Doped Tin Oxide Films. *Thin Solid Films* **2006**, *515*, 2678–2685.

- (21) Senguttuvan, T. D.; Malhotra, L. K. Sol Gel Deposition of Pure and Antimony Doped Tin Dioxide Thin Films by Non Alkoxide Precursors. *Thin Solid Films* **1996**, *289*, 22–28.

- (22) Jain, G.; Kumar, R. Electrical and Optical Properties of Tin Oxide and Antimony Doped Tin Oxide Films. *Opt. Mater.* **2004**, *26*, 27–31.
- (23) Babar, A. R.; Shinde, S. S.; Moholkar, A. V.; Bhosale, C. H.; Kim, J. H.; Rajpure, K. Y. Physical Properties of Sprayed Antimony Doped Tin Oxide Thin Films: The Role of Thickness. *J. Semicond.* **2011**, *32*, 053001.
- (24) Bhat, J. S.; Maddani, K. I.; Karguppikar, A. M. Influence of Zn doping on Electrical and Optical Properties of Multilayered Tin Oxide Thin Films. *Bull. Mater. Sci.* **2006**, *29*, 331–337.
- (25) Vijayalakshmi, S.; Venkataraj, S.; Subramanian, M.; Jayavel, R. Physical Properties of Zinc Doped Tin Oxide Films Prepared by Spray Pyrolysis Technique. *J. Phys. D: Appl. Phys.* **2008**, *41*, 035505.
- (26) Chandra, R. D.; Rao, M.; Zhang, K.; Prabhakar, R. R.; Shi, C.; Zhang, J.; Mhaisalkar, S. G.; Mathews, N. Tuning Electrical Properties in Amorphous Zinc Tin Oxide Thin Films for Solution Processed Electronics. *ACS Appl. Mater. Interfaces* **2014**, *6*, 773–777.
- (27) Koebel, M. M.; Nadargi, D. Y.; Jimenez-Cadena, G.; Romanyuk, Y. E. Transparent, Conducting ATO Thin Films by Epoxide-Initiated Sol–Gel Chemistry: A Highly Versatile Route to Mixed-Metal Oxide Films. *ACS Appl. Mater. Interfaces* **2012**, *4*, 2464–2473.
- (28) Du, J.; Chen, X.-l.; Liu, C.-c.; Ni, J.; Hou, G.-f.; Zhao, Y.; Zhang, X.-d. Highly Transparent and Conductive Indium Tin Oxide Thin Films for Solar Cells Grown by Reactive Thermal Evaporation at Low Temperature. *Appl. Phys. A: Mater. Sci. Process.* **2014**, *117*, 815–822.
- (29) Jiang, Y.; Sun, W.; Xu, B.; Yan, M.; Bahlawane, N. Unusual Enhancement in Electrical Conductivity of Tin Oxide Thin Films with Zinc Doping. *Phys. Chem. Chem. Phys.* **2011**, *13*, 5760–5763.
- (30) Klein, A.; Körber, C.; Wachau, A.; Säuberlich, F.; Gassenbauer, Y.; Harvey, S. P.; Proffit, D. E.; Mason, T. O. Transparent Conducting Oxides for Photovoltaics: Manipulation of Fermi Level, Work Function and Energy Band Alignment. *Materials* **2010**, *3*, 4892–4914.
- (31) Chen, Z.; Li, W.; Li, R.; Zhang, Y.; Xu, G.; Cheng, H. Fabrication of Highly Transparent and Conductive Indium-Tin Oxide Thin Films with a High Figure of Merit via Solution Processing. *Langmuir* **2013**, *29*, 13836–13842.
- (32) Choi, S.-I.; Nam, K. M.; Park, B. K.; Seo, W. S.; Park, J. T. Preparation and Optical Properties of Colloidal Monodisperse and Highly Crystalline ITO Nanoparticles. *Chem. Mater.* **2008**, *20*, 2609–2611.
- (33) Lu, P.-F.; Shen, Y.; Yu, Z.-Y.; Zhao, L.; Li, Q.-Y.; Ma, S.-J.; Han, L.-H.; Liu, Y.-M. Electronic Structure and Optical Properties of Antimony-Doped SnO<sub>2</sub> from First-Principle Study. *Commun. Theor. Phys.* **2012**, *57*, 145–150.
- (34) Dey, A. Semiconductor Metal Oxide Gas Sensors: A Review. *Mater. Sci. Eng., B* **2018**, *229*, 206–217.
- (35) Dagherir, R.; Drogui, P.; Robert, D. Modified TiO<sub>2</sub> For Environmental Photocatalytic Applications: A Review. *Ind. Eng. Chem. Res.* **2013**, *52*, 3581–3599.
- (36) Li, C.-H.; Li, M.-C.; Liu, S.-P.; Jamison, A. C.; Lee, D.; Lee, T. R.; Lee, T.-C. Plasmonically Enhanced Photocatalytic Hydrogen Production from Water: The Critical Role of Tunable Surface Plasmon Resonance from Gold–Silver Nanoshells. *ACS Appl. Mater. Interfaces* **2016**, *8*, 9152–9161.
- (37) Ohtani, B. Titania Photocatalysis beyond Recombination: A Critical Review. *Catalysts* **2013**, *3*, 942–953.
- (38) Unlu, I.; Soares, J. W.; Steeves, D. M.; Whitten, J. E. Photocatalytic Activity and Fluorescence of Gold/Zinc Oxide Nanoparticles Formed by Dithiol Linking. *Langmuir* **2015**, *31*, 8718–8725.
- (39) Jiang, T.; Qin, X.; Sun, Y.; Yu, M. UV Photocatalytic Activity of Au@ZnO Core-Shell Nanostructure with Enhanced UV Emission. *RSC Adv.* **2015**, *5*, 65595–65599.
- (40) Benjwal, P.; Kar, K. K. Removal of Methylene Blue from Wastewater under a Low Power Irradiation Source by Zn, Mn Co-Doped TiO<sub>2</sub> Photocatalysts. *RSC Adv.* **2015**, *5*, 98166–98176.
- (41) Naraginti, S.; Li, Y.; Wu, Y. A Visible Light Mediated Synergistic Catalyst for Effective Inactivation of E. Coli and Degradation of Azo Dye Direct Red-22 with Mechanism Investigation. *RSC Adv.* **2016**, *6*, 75724–75735.
- (42) Lin, X.; Fu, D.; Hao, L.; Ding, Z. Synthesis and Enhanced Visible-Light Responsive of C,N,S-Tridoped TiO<sub>2</sub> Hollow Spheres. *J. Environ. Sci.* **2013**, *25*, 2150–2156.
- (43) Choudhury, B.; Dey, M.; Choudhury, A. Shallow and Deep Trap Emission and Luminescence Quenching of TiO<sub>2</sub> Nanoparticles on Cu Doping. *Appl. Nanosci.* **2014**, *4*, 499–506.
- (44) Chiu, Y.-H.; Lai, T.-H.; Chen, C.-Y.; Hsieh, P.-Y.; Ozasa, K.; Niinomi, M.; Okada, K.; Chang, T.-S. M.; Matsushita, N.; Sone, M.; Hsu, Y.-J. Fully Depleted Ti-Nb-Ta-Zr-O Nanotubes: Interfacial Charge Dynamics and Solar Hydrogen Production. *ACS Appl. Mater. Interfaces* **2018**, *10*, 22997–23008.
- (45) Lu, Y.-H.; Lin, W.-H.; Yang, C.-Y.; Chiu, Y.-H.; Pu, Y.-C.; Lee, M.-H.; Tseng, Y.-S.; Hsu, Y.-J. A Facile Green Antisolvent Approach to Cu<sup>2+</sup>-Doped ZnO Nanocrystals with Visible-Light-Responsive Photoactivities. *Nanoscale* **2014**, *6*, 8796–8803.
- (46) Pu, Y.-C.; Chen, Y.-C.; Hsu, Y.-J. Au-Decorated Na<sub>2</sub>H<sub>2-x</sub>Ti<sub>3</sub>O<sub>7</sub> Nanobelts Exhibiting Remarkable Photocatalytic Properties under Visible-Light Illumination. *Appl. Catal., B* **2010**, *97*, 389–397.
- (47) Gaber, A.; Abdel-Latief, A. Y.; Abdel-Rahim, M. A.; Abdel-Salam, M. N. Thermally Induced Structural Changes and Optical Properties of Tin Dioxide Nanoparticles Synthesized by a Conventional Precipitation Method. *Mater. Sci. Semicond. Process.* **2013**, *16*, 1784–1790.
- (48) Gaber, A.; Abdel-Rahim, M. A.; Y, A.-L. A.; Abdel-Salam, M. N. Influence of Calcination Temperature on the Structure and Porosity of Nanocrystalline SnO<sub>2</sub> Synthesized by a Conventional Precipitation method. *Int. J. Electrochem. Sci.* **2014**, *9*, 81–95.
- (49) Salavati-Niasari, M.; Mir, N.; Davar, F. Synthesis, Characterization and Optical Properties of Tin Oxide Nanoclusters Prepared from a Novel Precursor via Thermal Decomposition Route. *Inorg. Chim. Acta* **2010**, *363*, 1719–1726.
- (50) Cerchier, P.; Dabalà, M.; Brunelli, K. Synthesis of SnO<sub>2</sub> and Ag Nanoparticles from Electronic Wastes with the Assistance of Ultrasound and Microwaves. *JOM* **2017**, *69*, 1583–1588.
- (51) Girão, H. T.; Cornier, T.; Daniele, S.; Debord, R.; Caravaca, M. A.; Casali, R. A.; Mélinon, P.; Machon, D. Pressure-Induced Disorder in SnO<sub>2</sub> Nanoparticles. *J. Phys. Chem. C* **2017**, *121*, 15463–15471.
- (52) Shaalan, N. M.; Hamad, D.; Abdel-Latief, A. Y.; Abdel-Rahim, M. A. Preparation of Quantum Size of Tin Oxide: Structural and Physical Characterization. *Prog. Nat. Sci.* **2016**, *26*, 145–151.
- (53) Miao, Z.; Wu, Y.; Zhang, X.; Liu, Z.; Han, B.; Ding, K.; An, G. Large-Scale Production of Self-Assembled SnO<sub>2</sub> Nanospheres and their Application in High-Performance Chemiluminescence Sensors for Hydrogen Sulfide Gas. *J. Mater. Chem.* **2007**, *17*, 1791–1796.
- (54) Volosin, A. M.; Sharma, S.; Traverse, C.; Newman, N.; Seo, D.-K. One-Pot Synthesis of Highly Mesoporous Antimony-Doped Tin Oxide from Interpenetrating Inorganic/Organic Networks. *J. Mater. Chem.* **2011**, *21*, 13232–13240.
- (55) Mani, R.; Vivekanandan, K.; Vallalperuman, K. Synthesis of Pure and Cobalt (Co) Doped SnO<sub>2</sub> Nanoparticles and its Structural, Optical and Photocatalytic Properties. *J. Mater. Sci.: Mater. Electron.* **2017**, *28*, 4396–4402.
- (56) Jia, X.; Liu, Y.; Wu, X.; Zhang, Z. A Low Temperature Situ Precipitation Route to Designing Zn-doped SnO<sub>2</sub> Photocatalyst with Enhanced Photocatalytic Performance. *Appl. Surf. Sci.* **2014**, *311*, 609–613.
- (57) Li, G.; Li, L.; Zheng, J. Understanding the Defect Chemistry of Oxide Nanoparticles for Creating New Functionalities: A Critical Review. *Sci. China: Chem.* **2011**, *54*, 876–886.
- (58) Li, C.-H.; Jamison, A. C.; Rittikulsittichai, S.; Lee, T.-C.; Lee, T. R. In Situ Growth of Hollow Gold–Silver Nanoshells within Pore Silica Offers Tunable Plasmonic Extinctions and Enhanced Colloidal Stability. *ACS Appl. Mater. Interfaces* **2014**, *6*, 19943–19950.

- (59) Oldfield, G.; Ung, T.; Mulvaney, P. Au@SnO<sub>2</sub> Core–Shell Nanocapacitors. *Adv. Mater.* **2000**, *12*, 1519–1522.
- (60) Choi, Y.-I.; Salman, S.; Kuroda, K.; Okido, M. Synergistic Corrosion Protection for AZ31 Mg Alloy by Anodizing and Stannate Post-Sealing Treatments. *Electrochim. Acta* **2013**, *97*, 313–319.
- (61) Rai, D.; Yui, M.; Schaef, H. T.; Kitamura, A. Thermodynamic Model for SnO<sub>2</sub> (cr) and SnO<sub>2</sub> (am) Solubility in the Aqueous Na<sup>+</sup>–H<sup>+</sup>–OH<sup>–</sup>–Cl<sup>–</sup>–H<sub>2</sub>O System. *J. Solution Chem.* **2011**, *40*, 1155–1172.
- (62) Garbassi, F. XPS and AES Study of Antimony Oxides. *Surf. Interface Anal.* **1980**, *2*, 165–169.
- (63) Bhagwat, A. D.; Sachin, S. S.; Balprasad, G. A.; Chandrashekar, M. M. Synthesis of Nanostructured Tin Oxide (SnO<sub>2</sub>) Powders and Thin Films by Sol-Gel Method. *J. Nano-Electron. Phys.* **2015**, *7*, 04037.
- (64) Senthilkumar, V.; Vickraman, P.; Ravikumar, R. Synthesis of Fluorine Doped Tin Oxide Nanoparticles by Sol–Gel Technique and their Characterization. *J. Sol-Gel Sci. Technol.* **2010**, *53*, 316–321.
- (65) Ayeshamariam, A.; Samy, R. P. Synthesis, Structural and Optical Characterizations of SnO<sub>2</sub> Nanoparticles. *Journal on Photonics and Spintronics* **2013**, *2*, 4–8.
- (66) Lim, H. N.; Nurzulaikha, R.; Harrison, I.; Lim, S. S.; Tan, W. T.; Yeo, M. C. Spherical Tin Oxide, SnO<sub>2</sub> Particles Fabricated via Facile Hydrothermal Method for Detection of Mercury (II) Ions. *Int. J. Electrochem. Sci.* **2011**, *6*, 4329–4340.
- (67) Abdel-latif, A. Y.; Abdel-Rahim, M. A.; Shaalan, N. M.; Hamad, D. Structural and Crystal Growth Kinetics Studies for SnO<sub>2</sub> Nanoparticles Prepared via Hydrothermal Route. *Phase Transit.* **2017**, *90*, 1214–1228.
- (68) Ravichandran, K.; Philominathan, P. Fabrication of Antimony Doped Tin Oxide (ATO) Films by an Inexpensive, Simplified Spray Technique using Perfume Atomizer. *Mater. Lett.* **2008**, *62*, 2980–2983.
- (69) Kumar Trivedi, M. The Potential Impact of Biofield Energy Treatment on the Physical and Thermal Properties of Silver Oxide Powder. *Int. J. Biomed. Sci. Eng.* **2015**, *3*, 62–68.
- (70) Chen, Y.; Qu, B.; Mei, L.; Lei, D.; Chen, L.; Li, Q.; Wang, T. Synthesis of ZnSnO<sub>3</sub> Mesocrystals from Regular Cube-like to Sheet-like Structures and their Comparative Electrochemical Properties in Li-Ion Batteries. *J. Mater. Chem.* **2012**, *22*, 25373–25379.
- (71) Ma, G.; Zou, R.; Jiang, L.; Zhang, Z.; Xue, Y.; Yu, L.; Song, G.; Li, W.; Hu, J. Phase-Controlled Synthesis and Gas-Sensing Properties of Zinc Stannate (ZnSnO<sub>3</sub> and Zn<sub>2</sub>SnO<sub>4</sub>) Faceted Solid and Hollow Microcrystals. *CrystEngComm* **2012**, *14*, 2172–2179.
- (72) Shannon, R. Revised Effective Ionic Radii and Systematic Studies of Interatomic Distances in Halides and Chalcogenides. *Acta Crystallogr., Sect. A: Cryst. Phys., Diffraction, Theor. Gen. Crystallogr.* **1976**, *32*, 751–767.
- (73) Khan, M. M.; Ansari, S. A.; Khan, M. E.; Ansari, M. O.; Min, B.-K.; Cho, M. H. Visible Light-Induced Enhanced Photoelectrochemical and Photocatalytic Studies of Gold Decorated SnO<sub>2</sub> Nanostructures. *New J. Chem.* **2015**, *39*, 2758–2766.
- (74) Tauc, J.; Grigorovici, R.; Vancu, A. Optical Properties and Electronic Structure of Amorphous Germanium. *Phys. Status Solidi B* **1966**, *15*, 627–637.
- (75) Kamble, V. B.; Umarji, A. M. Defect Induced Optical Bandgap Narrowing in Undoped SnO<sub>2</sub> Nanocrystals. *AIP Adv.* **2013**, *3*, 082120.
- (76) Serpone, N. Is the Band Gap of Pristine TiO<sub>2</sub> Narrowed by Anion- and Cation-Doping of Titanium Dioxide in Second-Generation Photocatalysts? *J. Phys. Chem. B* **2006**, *110*, 24287–24293.
- (77) Zak, A. K.; Razali, R.; Majid, W. H. A.; Darroudi, M. Synthesis and Characterization of a Narrow Size Distribution of Zinc Oxide Nanoparticles. *Int. J. Nanomed. B* **2011**, *6*, 1399–1403.
- (78) Wochnik, A. S.; Handloser, M.; Durach, D.; Hartschuh, A.; Scheu, C. Increasing Crystallinity for Improved Electrical Conductivity of TiO<sub>2</sub> Blocking Layers. *ACS Appl. Mater. Interfaces* **2013**, *5*, 5696–5699.
- (79) Ni, Y.; Zhu, Y.; Ma, X. A Simple Solution Combustion Route for the Preparation of Metal-Doped TiO<sub>2</sub> Nanoparticles and their Photocatalytic Degradation Properties. *Dalton Trans.* **2011**, *40*, 3689–3694.
- (80) Brokken-Zijp, J. C. M.; van Asselen, O. L. J.; Kleinjan, W. E.; Van De Belt, R.; De With, G. Photocatalytic Properties of Tin Oxide and Antimony-Doped Tin Oxide Nanoparticles. *J. Nanotechnol.* **2011**, *2011*, 106254.